Drastic modification of Low Temperature Thermoelectric Properties of Na-doped $Bi_2Sr_2Co_2O_y$ Ceramics Prepared via Laser Floating Zone Technique

G. Çetin*[1], B. Özçelik[1], M. Gürsul[1], M. A. Madre[2], A. Sotelo[2], S.Adachi[3], Y.Takano[3]

[1]Department of Physics, Faculty of Sciences and Letters, Çukurova University, 01330 Adana, (Turkey).

[2]ICMA (CSIC-Universidad de Zaragoza), C/María de Luna 3, 50018-Zaragoza (Spain).

[3]National Institute for Materials Science, 1-2-1 Sengen, Tsukuba, Ibaraki 305-0047, Japan

Abstract

In this study, $Bi_2Sr_{2-x}Na_xCo_2O_y$ (x= 0.0, 0.05, 0.075, 0.10, and 0.15) ceramic powders have been fabricated via the classical ceramic route, followed by a texturing process through the laser floating zone (LFZ) technique. XRD patterns show the thermoelectric phase as the major one. In addition, Na-substitution reduces the amount of secondary phases, when compared to the pure sample. SEM observations point out that grain orientation is significantly improved when Na-content is increased. Na-substitution reduces electrical resistivity from 35mΩ.cm (in pure samples) to 19.6 mΩ.cm (in Na=0.05 ones) at around room temperature, while Seebeck coefficient is, approximately, twice the measured in Na-free ones. On the other hand, thermal conductivity is slightly lower in undoped samples (0.83 W/K m), when compared to the Na-substituted ones (1.10-1.40 W/K m) at room temperature, due to their lower electrical conductivity. Finally, ZT values are higher when the Na-content is increased, reaching 0.022 at around 400 K.

Keywords: Thermoelectric oxides; Texture; Microstructure; Electrical properties; Figure of Merit

Corresponding author: Tel./fax:+90.322.3386080/+90.322.3386070
e-mail: gcetin@cu.edu.tr

1. Introduction

Research on alternative energy sources is quite popular due to challenges like the decrease of fossil-fuel-based energy sources, increase in energy demand and global warming. Thermoelectric materials have an important place in this kind of research in order to enable the reuse of waste heat as electrical energy. These materials allow producing electric energy from a temperature gradient when they are integrated into thermoelectric generators formed by p-n legs. The conversion efficiency of these materials can be obtained from the dimensionless figure of merit, *ZT*, defined as $TS^2/\rho\kappa$, where T is the absolute temperature, S Seebeck coefficient, ρ electrical resistivity, and κ thermal conductivity [1]. Bi_2Te_3, PbTe and $CoSe_3$ intermetallics are commonly used as thermoelectric materials in commercial modules. However, this compounds show some important drawbacks such as their low abundance in the earth's crust [2], and their degradation and/or liberation of heavy elements at high temperatures under air [3]. Such problems have caused the emergence of Co-based oxides, which are abundant in earth's crust, stable at high temperatures, and much less toxic. The first discovered member of this CoO-based family, Na_xCoO_2, exhibits large termoelectric power, breaking the general belief that oxides had poor thermoelectric properties [4]. This work led to the discovery of new layered cobaltites with p-type behavior, such as Ca-Co-O [5], Bi-Ca-Co-O [6], and Bi-Sr-Co-O [7]. In addition, other families as TiO- and MnO-based materials [8,9] were discovered, exhibiting n-type properties, being the counterpart of p-type ones in thermoelectric modules.

Various crystallographic studies showed that Co-based crystal structure can be described as composed of two different layers, namely CdI_2-type CoO_2 conductive layer and rock salt (RS) $Bi_2X_2O_4$ (X=Ca, Sr and Ba) insulating layers. These two layers have common ***a***- and ***c***-axis lattice parameters with different ***b***-axis length, which causes a misfit along the ***b***-direction [10,11]. This irregularity in the crystal structure causes a high anisotropy in the material as well as in its electrical properties and Seebeck coefficient. In this regard, cation substitution [12-15] or different synthesis techniques [16-19] have been performed to enhance thermoelectric properties of these materials. Taking into account these previous studies, the aim of this work is investigating the effect of Na substitution for Ca on the microstructure, and thermoelectric and magnetic properties of $Bi_2Sr_2Co_2O_y$ prepared by solid state method followed by LFZ texturing.

2. Experimental Procedure

$Bi_2Sr_{2-x}Na_xCo_2O_y$ (x= 0, 0.05, 0.075, 0.10, and 0.15) thermoelectric ceramics were prepared via the conventional solid state method using Bi_2O_3, $SrCO_3$, Na_2CO_3, and CoO commercial powders. In a first step, they were homogenously mixed and-ball milled for 30 min. at 300 rpm in distilled water media. Then, infrared lamps were used to dry the suspension and manually milled to break the agglomerates. The resulting homogenous mixtures were calcined twice at 750 and 800°C to decompose CO_2 from the metallic carbonates and isostatically pressed into cylindrical rods with radius φ=2-3mm, and ~100mm length under 200 MPa. These rods were finally used as feed in LFZ system powered with Nd-YAG laser radiation (λ=1064nm) [20]. The grown speed of all samples has been 30 mm/h, with 3 rpm seed rotation to obtain the cylindrical geometry. At the same time, the feed was oppositely rotated at 15 rpm to obtain a homogeneous molten zone. This process leads to very dense and geometrically homogeneous cylindrical rods with around 2.5 mm diameter. However, due to its incongruent melting, several secondary phases are also formed after LFZ process, besides the thermoelectric one [21, 22]. Therefore, a final heat treatment at 810°C for 24h was applied to reduce the secondary phases content, increasing the thermoelectric phase proportion in the samples. Consequently, all characterizations have been performed on textured and annealed samples.

Structural features have been determined through the powder XRD technique with 2θ between 5 and 40 degrees. In order to evaluate the microstructure of $Bi_2Sr_{2-x}Na_xCo_2O_y$ samples a field emission scanning electron microscope (FESEM, Zeiss Merlin), with an attached EDS system, was used. For these observations, longitudinal polished sections of samples were prepared by hot-embedding the fibers into conducting resin, grinded to reach their center, and finally polished with diamond paste. Density of samples has also been determined through Archimedes method, taking 6.8 g/cm^{3}as theoretical density [23]. ρ, κ and S have been simultaneously measured from 4.2–390 K in a Quantum Design PPMS system. Figure of Merit, ZT (= $S^2T/\rho\kappa$), was calculated to establish the thermoelectric performances of these samples as a function of temperature and Na content.

3. Results and Discussion:

Powder XRD patterns were acquired at room temperature and illustrated in Fig.1. Regardless of Na content, all patterns are quite similar and major peaks correspond to the thermoelectric phase. In the graph, plane reflections for the thermoelectric phase have been labeled, and most of them correspond to the *(00l)* planes, in agreement with previously reported data [24, 25]. In addition, small amount of secondary phases, such as $Bi_{0.75}Sr_{0.25}O_y$, $CoCo_2O_4$ (identified as *, and #, respectively), were observed due to their incongruent melting. Moreover, when Na content is increased, the amount of these phases is decreased, without observing any Na-based phases. Hence, it can be concluded that Na ions are incorporated into the TE phase, and also decreases secondary phases content.

Representative SEM micrographs of samples after the growth process and presented in Fig. 2. They show several contrasts: Black (#1), dark grey (#2), grey (#3), light grey (#4) and white (#5), which have been identified through EDS as Co oxide, Bi poor phase, TE phase ($Bi_2Sr_{2-x}Na_xCo_{1.8}O_y$), $Bi_2Sr_2Co_1O_x$, and Bi/Sr rich oxide, respectively. The compositional variation of the thermoelectric phase in the textured annealed samples with the Na nominal substitution, is displayed in Table 1. As it can be observed in this table, Na content is slightly lower than the nominal one, probably due to volatilization of Na_2CO_3 during the laser texturing process. In general, volatilization of the molten Na_2CO_3 is known as one the factors that limit the performance of molten carbonate fuel cells (MCFC), even operating at lower temperatures [26]. On the other hand, it is clear that the secondary phases proportion decreases when the Na content is increased, in agreement with XRD results. Furthermore, increasing Na-content, better grain orientation is produced, due to the fact that introducing Na decreases the melting point of the samples, and reduces the radial thermal gradient in the solidification interface, as observed in similar systems [27].

Fig. 3 presents electrical resistivity curves between 5 and 390 K for $Bi_2Sr_{2-x}Na_xCo_2O_y$. At low temperatures, all samples display semiconducting-like behavior ($d\rho/dt<0$), reaching the minimum at the metal-insulator-transition-temperature (T_{min}). This transition temperature is increased when the Na content is raised, implying the occurrence of ordering in the incommensurate spin-density-wave (IC-SDW) [28]. After this minimum, metallic like behavior is presented ($d\rho/dt>0$) up to the so-called T^* temperature, determining the transition from a strongly correlated Fermi liquid regime to incoherent metal regime [29], and suggesting the existence of mobile carriers. T_{min}, T^* and room temperature resistivity values are tabulated in Table 2. As it can be seen in the table, the room temperature resistivity of all doped samples is much smaller than those determined in the undoped ones. In addition, T_{min} and T^* values monotonically increase with increasing Na-content. The evolution of these resistivity results can be explained by the reduction of the oxidation state in the rock salt layer provided by the replacement of Sr^{2+} with Na^+. As a consequence, some Co^{3+} is raised to Co^{4+}, in order to preserve electrical neutrality of the structure, increasing the charge carrier concentration and decreasing resistivity. While room-temperature resistivity value is around 35mΩ.cm for undoped samples, this value decreases to 21.2 mΩ.cm for x=0.15 and 19.6 mΩ.cm for x=0.05 samples. Variable range hopping (VRH) [17] model can be used at low temperatures to describe the resistivity behavior of samples. In this model, resistivity variation with temperature can be described as:

$$\rho(T) = \rho(0)\ exp\ (T_0/T)^{1/3} \qquad (1)$$

where, T_0 is the characteristic temperature of VRH model, given as $T_0 = 8/[\pi k_B N(\varepsilon_F) l_v^2]$, in which $N(\varepsilon_F)$ is the density of localized states at Fermi level, k_B is Boltzmann constant and l_v is the localization length [30]. T_0 value can be obtained from the slope of $ln\rho(T)$ -$T^{1/3}$ graph as shown in Figure 4a. T_0 values are listed in Table 2, where it can be observed that they increase with increasing Na-content, and implying the decrease of localization length, l_v.

At higher temperatures, the thermal energy increased, exciting holes carriers, and then VRH model is not sufficient to describe the samples behavior. Instead, thermally activated conduction (TAC) model [29,30] can be used with the following expression:

$$\frac{1}{\rho} = \mu(T)\ exp\left(-\frac{E_0}{k_B}\right) \qquad (2)$$

which can be rewritten as;

$$ln\rho = \frac{E_0}{k_B}T^{-1} - ln\mu = AT^{-1} + B \qquad (3)$$

where $\mu(T)$ is charge carriers mobility, k_B is the Boltzmann constant, E_0 is the energy gap or activation energy due to the spin density wave (SDW) occurring at Fermi surface with fitting parameters A and B. By using this equation, low resistivity data was fitted and presented in Fig. 4b. The slope in the plots of $ln\ \rho$ versus T^{-1} corresponds to the samples activation energy (E_0). As it can be seen, the obtained E_0 values increase with increasing Na-content, suggesting that replacing Ca with Na positively affects the formation of the SDW propagating in the CoO_2 plane. Furthermore, the increase in the activation energy can be an indication of the Co^{+3} to Co^{+4} promotion. Hence, introducing Na into the rock salt layer has an indirect effect on the CoO$_2$ plane promoting SDW state surviving in the CoO$_2$ plane.

The temperature dependence of Seebeck coefficient as a function of Na-content is presented in Fig. 5. At a first sight, Seebeck coefficient is positive for all samples in the whole measured temperature range which is indicative of p-type conduction. More importantly, Seebeck coefficient of Na-doped samples is increased, approximately, twice compared to Na-free samples. A temperature independent expression for the Seebeck coefficient is given by Koshibae et al. [31] as follows;

$$S=-\frac{k_B}{|e|}\ln\left(\frac{1}{6}\frac{x}{1-x}\right) \qquad (4)$$

where k_B is the Boltzmann constant, e is the electron charge and x is the concentration of Co^{+4} ions. The Seebeck coefficient at room temperature is around 110 μV/K for all Na-doped samples and 55 μV/K for Na-free sample. This Seebeck coefficient increase can be attributed to the higher concentration of Co^{+4} ions given in the Koshibae's equation. By using this equation, the valence of cobalt ions is approximately 3.45 at around 300K for Na-doped samples. However, this model is not realistic enough as it is ignoring the peculiar splitting of the t_{2g} levels in the CoO$_2$ layer [32]. As a matter of fact, Seebeck coefficient of Na-doped samples increases almost linearly up to 300K indicating a temperature dependency. A temperature dependent expression for Seebeck effect is given by the Mott formula [30];

$$S=\frac{C_e}{n}+\frac{T\pi^2k_B^2}{3e}\left[\frac{\partial\, ln\mu(\varepsilon)}{\partial\varepsilon}\right] \qquad (5)$$

where n, C_e, k_B, and $\mu(\varepsilon)$ are carrier concentration, electronic specific heat, Boltzmann constant, and energy correlated mobility, respectively. By using this relation, it can be suggested that an increase in carrier concentration reduces Seebeck coefficient as indicated by the first term in Eq. 5. Therefore, the increase in the Seebeck coefficient with Na-content can be explained by the second term in Eq. 5. By increasing Na-content, due to the disorder arising from Na substitution, the rate of change in the system energy correlated mobility is increased, leading to higher Seebeck coefficient values. At room temperature, the S values change from 54 μV/K (pure samples) to 115 μV/K (0.075 Na doped samples).

Fig. 6 presents thermal conductivity, $\kappa(T)$, versus temperature curves for the samples. According to the graph, the thermal conductivity behavior of all samples seems very similar.

It increases linearly with temperature at low temperatures, and tends to be almost temperature independent at higher ones. Generally, thermal conductivity can be expressed as [33];

$$\kappa(T) = \kappa_{ph}(T) + \kappa_{ch}(T) \tag{6}$$

where $\kappa_{ph}(T)$ and $\kappa_{ch}(T)$ are phonon, and carrier thermal conductivity components, respectively. In this expression $\kappa_{ch}(T)$ term can be deduced from Wiedemann-Franz (W-F) law given as $\kappa_{ch}(T)=LT/\rho$ where L is the Lorentz number with the value of 2.45×10^{-8} V^2/K^2. Calculated κ_{ch} values at room temperature are presented in Table 2. These values are around 0.03 in all cases, being slightly higher for Na doped samples. Tipycally, the contribution of carrier thermal conductivity component is small, and the main contribution comes from the phonon thermal conductivity component. In addition, the difference between the ionic radii of the Na and Sr affects the lattice vibrations positively by distorting the crystal lattice.

In order to determine TE performances of the samples ZT has been calculated from ρ, S and κ values, and plotted, as a function of temperature, in Fig. 7. Although all Na-substituted samples possess higher thermal conductivity, ZT values of all Na-substituted samples are higher than the obtained in Na-free ones. The largest ZT value has been obtained for x=0.15 sample (0.017) at room temperature. This value is higher than the reported for melt quenched samples (0.010) [34], and in the same order of those obtained in spark plasma textured materials [35].

Temperature dependence of magnetization between 5-300K for all samples is presented in Fig. 8. From the figure, it can be seen that magnetization behavior of all samples are quite similar, sharply increasing below 50 K. At higher temperatures, temperature dependence of magnetization is relatively weak and shows a temperature-independent tendency with temperature. The fitted line in the graph of the $1/\chi$ versus T given in the inset of Fig. 8 cuts the temperature axis at negative temperatures. This means that antiferromagnetic-type interactions are dominant at low temperatures. The magnetic field dependence of magnetization curves for $BiSr_{2-x}Na_xCo_2O_y$ fibers under up to $\pm 5T$ applied fields at 10K are displayed in Fig. 9. In the figure, it can be observed that the behavior of all curves is similar and no hysteresis behavior can be observed, which indicates paramagnetic behavior at higher temperatures.

4. Conclusion

In this study, $Bi_2Sr_{2-x}Na_xCo_2O_y$ ceramics were produced via the conventional solid state method and textured using the LFZ technique. XRD patterns showed that major phase is the thermoelectric one regardless of Na concentration. SEM-EDS analysis have shown that Na doping enhances grain orientation and slightly decreases the amount of secondary phases. Samples resistivity is decreased with Na-content, and a broad minimum at T_{min} can be observed in all samples, implying the presence IC-SDW ordering. Seebeck coefficient of Na-doped samples increased approximately twice compared to Na-free ones. Although doped samples possess higher thermal conductivity, due to their lower resistivity and higher Seebeck coefficient, ZT values of all doped samples are higher than for Na-free ones.

Acknowlegements.

This work is supported by Research Fund of Çukurova University, Adana, Turkey, under grant contracts no: FDK-2016-6105 and FBI-2017-9225. M. A. Madre and A. Sotelo wish to thank the Gobierno de Aragón-FEDER (Research Group T 54-17 R), and the Spanish MINECO-FEDER (MAT2017-82183-C3-1-R) for financial support. The use of Servicio General de Apoyo a la Investigación-SAI, Universidad de Zaragoza is also acknowledged.

References:

[1] D.M. Rowe, in: D.M. Rowe (Ed.), Thermoelectrics Handbook: Macro to Nano, 1st edn, CRC Press, Boca Raton, FL, 2006, pp. 1–3.

[2] A.A. Yaroshevsky, Abundances of chemical elements in the Earth's crust Geochem. Int.44 (2006) 48–55.

[3] M.H. Elsheikh, D.A.Shnawah, M.F.M.Sabri, S.B.M.Said, M.H.Hassan, M.B.A. Bashir, M.Mohamad, A review on thermoelectric renewable energy: principle parameters that affect their performance, Renew.Sust. Energy Rev30 (2014) 337–355.

[4] I. Terasaki, Y. Sasago, K. Uchinokura, Large thermoelectric power in $NaCo_2O_4$ single crystals, Phys. Rev. B 56 (1997) R12685.

[5] S.W. Li, et al. J. Mater. Chem. 9, 1659 (1999)

[6] A. Maignan, et al. J. Phys.:Condens. Matter 15, 2711 (2003)

[7] R. Funahashi, et al. Appl. Phys. Lett. 76 2385 (200)

[8] H. Wang, C.L. Wang, Thermoelectric properties of Yb-doped $La_{0.1}Sr_{0.9}TiO_3$ ceramics at high temperature, Ceram. Int. 39 (2013) 941–946.

[9] Y.H. Zhu, W.B. Su, J. Liu, Y.C. Zhou, J. Li, X. Zhang, Y. Du, C.L. Wang, Effects of Dy and Yb co-doping on thermoelectric properties of $CaMnO_3$ ceramics, Ceram. Int. 41 (2015) 1535–1539.

[10] Y. Miyazaki, Crystal structure and thermoelectric properties of the misfit-layered cobalt oxides, Solid State Ion. 172 (2004) 463.

[11] H. Leligny, D. Grebille, O. Perez, A.C. Masset, M. Hervieu, B. Raveau, A five-dimensional structural investigation of the misfit layer compound $[Bi_{0.87}SrO_2]_2[CoO_2]_{1.82}$, Acta Cryst. B 56 (2000) 173.

[12] H.S. Hao, Q.L. He, L.M. Zhao, Thermoelectric properties of Cu-substituted $Bi_2Ca_2Co_2O_y$ misfit oxides, Adv. Mater. Res. 284-286 (2011) 2263.

[13] G. Constantinescu, M.A. Torres, Sh. Rasekh, J.C. Diez, M.A. Madre, A. Sotelo, Effect of Sr substitution for Ca on the $Ca_3Co_4O_9$ thermoelectric properties, J. Alloys Compd. 577 (2013) 511–515.

[14] G. Çetin Karakaya, B. Özçelik, M.A. Torres, M.A. Madre, A. Sotelo, Effects of K substitution on thermoelectric and magnetic properties of $Bi_2Sr_2Co_2O_y$ ceramic, J. Mater. Sci. Mater. Electron. 28 (2017) 12652.

[15] N. Sun, S. T. Dong, B.B. Zhang, Y.B. Chen, J. Zhou, S.T.Zhang, Z.B. Gu,S.H. Yao, Y.F. Chen, Intrinsically modified thermoelectric performance of alkaline-earth isovalently substituted $[Bi_2AE_2O_4][CoO_2]_y$ single crystals, J.Appl.Phys.114 (2013) 043705.

[16] Y. Zhang, J. Zhang, Q. Lu, Synthesis of highly textured $Ca_3Co_4O_9$ ceramics by spark plasma sintering, Ceram. Int. 33 (2007) 1305.

[17] H. Itahara, C. Xia, J. Sugiyama, T. Tani, Fabrication of textured thermoelectric layered cobaltites with various rock salt-type layers by using β-Co(OH)2 platelets as reactive templates, J. Mater. Chem. 14 (2004) 61.

[18] J.G. Noudem, D. Kenfaui, D. Chateigner, M. Granular Gomina, Lamellar thermoelectric oxides consolidated by spark plasma sintering, J. Korean Inst. Electr. Electron. Mater. Eng. 40 (2011) 1100.

[19] N.M. Ferreira, F.M. Rasekh Sh Costa, M.A. Madre, A. Sotelo, J.C. Diez, M.A. Torres, New method to improve the grain alignment and performance of thermoelectric ceramics, Mater. Lett. 83 (2012) 144–147.

[20] A. Sotelo, G. Rasekh Sh Constantinescu, M.A. Torres, M.A. Madre, J.C. Diez, Improvement of textured $Bi_{1.6}Pb_{0.4}Sr_2Co_{1.8}O_x$ thermoelectric performances by metallic Ag additions, Ceram. Int. 39 (2013) 1597–1602.

[21] S.h. Rasekh, F.M. Costa, N.M. Ferreira, M.A. Torres, M.A. Madre, J.C. Diez, A. Sotelo, Use of laser technology to produce high thermoelectric performances in $Bi_2Sr_2Co_{1.8}O_x$, Mater. Design 75 (2015) 143.

[22] E. Combe, R. Funahashi, T. Barbier, F. Azough, R. Freer, Decreased thermal conductivity in $Bi_2Sr_2Co_2O_x$ bulk materials prepared by partial melting, J. Mater. Res. 31 (2016) 1296.

[23] E. Combe, R. Funahashi, T. Barbier, F. Azough, R. Freer, Decreased thermal conductivity in $Bi_2Sr_2Co_2O_x$ bulk materials prepared by partial melting, J. Mater. Res. 31 (2016) 1296.

[24] A. Sotelo, Sh. Rasekh, G. Constantinescu, M.A. Torres, M.A. Madre, J.C. Diez Improvement of textured $Bi_{1.6}Pb_{0.4}Sr_2Co_{1.8}O_x$ thermoelectric performances by metallic Ag additions, Ceramics International 39 (2013) 1597–1602.

[25] M. Kato, Y. Goto, K. Umehara, K. Hirota, I. Terasaki, Synthesis and physical properties of Bi–Sr–Co–oxides with 2D-triangular Co layers intercalated by iodine, Physica B 378–380 (2006) 1062–1063.

[26] K. Sugiura, M. Yamauchi, K. Tanimoto, Y. Yoshitani, Evaluation of volatile behaviour and the volatilization volume of molten salt in DIR-MCFC by using the image measurement technique, J. Power Sources 145 (2005) 199.

[27] F.M. Costa, N.M. Ferreira, S.h. Rasekh, A.J.S. Fernandes, M.A. Torres, M.A. Madre, J.C. Diez, A. Sotelo, Very large superconducting currents induced by growth tailoring, Cryst. Growth Des. 15 (2015) 2094.

[28] J. Sugiyama, H. Itahara, T. Tani, J.H. Brewer, E.J. Ansaldo, Magnetism of layered cobalt oxides investigated by muon spin rotation and relaxation, Phys. Rev. B 66 (2002) 134413.

[29] Y. Huang, B. Zhao, R. Ang, S. Lin, Z. Huang, S. Tan, Y. Liu, W. Song, Y. Sun, Enhanced thermoelectric performance and room-temperature spin-state transition of Co^{4+} ions in the $Ca_3Co_{4-x}Rh_xO_9$ system, J. Phys. Chem. C 117 (2013) 11459.

[30] N.F. Mott, E.A. Davis, Electronic Processes in Non-Crystalline Materials, Clarendon Press, London, 1971.

[31] W. Koshibae, K. Tsuitsui, S. Maekawa, Thermopower in cobalt oxides, Phys.Rev. B 62 (2000) 6869

[32] L.H. Yin, R. Ang, L.J. Li, B.C. Zhao, Y.K. Fu, X.B. Zhu, Z.R. Yang, W.H. Song, Y.P. Sun, Thermoelectric properties of sol–gel derived cobaltite $Bi_2Ca_{2.4}Co_2O_y$, Physica B 406 (2011) 2914.

[33] Y. Wang, Y. Sui, X.J. Wang, W.H. Su, X.Y. Liu, Enhanced high temperature thermoelectric characteristics of transition metals doped $Ca3Co4O9+\delta$ by cold high pressure fabrication, J. Appl. Phys. 107 (2010) 033708.

[34] J. Lingner, R. Funahashi, E. Combe, M. Letz, G. Jakob, Thermoelectric sintered glass-ceramics with a $Bi_2Sr_2Co_2O_x$ phase, Appl. Phys. A 120 (2015) 59.

[35] K. Rubesova, T. Hlasek, V. Jakes, S. Huber, J. Hejtmanek, D. Sedmidubsky, Effect of a powder compaction process on the thermoelectric properties of $Bi_2Sr_2Co_{1.8}O_x$ ceramics, J. Eur. Ceram. Soc. 35 (2015) 525.

Table 1. Cationic composition of the thermoelectric phase as a function of the nominal Na substitution obtained through EDS

Nominal Na content	**Bi**	**Sr**	**Na**	**Co**
0.0	2.0	1.9	0.0	1.8
0.05	2.1	1.8	0.03	1.8
0.075	2.1	1.8	0.06	1.8
0.10	2.0	1.9	0.09	1.8
0.15	2.0	1.8	0.12	1.8

Table 2. Electrical and thermal transport parameters for all $Bi_2Sr_{2-x}Na_xCo_2O_y$ samples

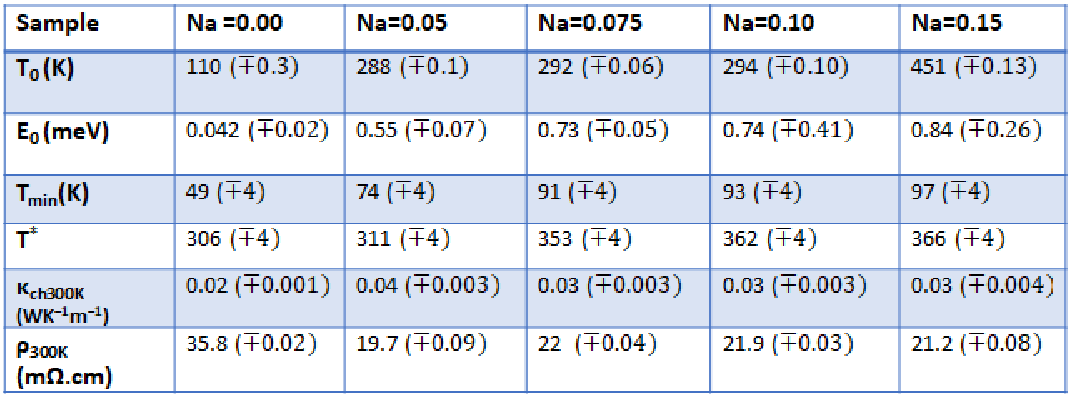

Sample	Na =0.00	Na=0.05	Na=0.075	Na=0.10	Na=0.15
T_0(K)	110 (∓0.3)	288 (∓0.1)	292 (∓0.06)	294 (∓0.10)	451 (∓0.13)
E_0(meV)	0.042 (∓0.02)	0.55 (∓0.07)	0.73 (∓0.05)	0.74 (∓0.41)	0.84 (∓0.26)
T_{min}(K)	49 (∓4)	74 (∓4)	91 (∓4)	93 (∓4)	97 (∓4)
T^*	306 (∓4)	311 (∓4)	353 (∓4)	362 (∓4)	366 (∓4)
κ_{ch300K} ($WK^{-1}m^{-1}$)	0.02 (∓0.001)	0.04 (∓0.003)	0.03 (∓0.003)	0.03 (∓0.003)	0.03 (∓0.004)
ρ_{300K} (mΩ.cm)	35.8 (∓0.02)	19.7 (∓0.09)	22 (∓0.04)	21.9 (∓0.03)	21.2 (∓0.08)

FIGURE CAPTIONS

Figure 1. XRD patterns of $Bi_2Sr_{2-x}Na_xCo_2O_y$ samples for x= (a) 0; (b) 0.05; (c) 0.075; (d) 0.10 and (e) 0.15. Diffraction planes identify the peaks associated to the thermoelectric phase, while ★ and # correspond to $Bi_{0.75}Sr_{0.25}O_y$, and $CoCo_2O_4$ secondary phases, respectively.

Figure 2. Representative SEM micrographs of $Bi_2Sr_{2-x}Na_xCo_2O_y$ samples for x= (***a***) 0; (***b***) 0.075, and (***c***) 0.15. Black (#1), dark grey (#2), grey (#3), light grey (#4) and white (#5) contrast correspond to Co oxide, Bi poor phase, TE phase ($Bi_2Sr_{2□x}Na_xCo_{1.8}O_y$), $Bi_2Sr_2Co_1O_x$ and Bi/Sr rich oxide, respectively.

Figure 3. Temperature dependence of electrical resistivity for $Bi_2Sr_{2-x}Na_xCo_2O_y$

Figure 4. (***a***) $\ln \rho$- $T^{-1/3}$ plots between 10 and 37K, (***b***) $\ln \rho$- T^{-1} plots between 12 and 380 K

Figure 5. Temperature dependence of Seebeck coefficient for $Bi_2Sr_{2-x}Na_xCo_2O_y$

Figure 6. Temperature dependence of thermal conductivity for $Bi_2Sr_{2-x}Na_xCo_2O_y$

Figure 7. ZT evolution with respect to temperature for $Bi_2Sr_{2-x}Na_xCo_2O_y$

Figure 8. DC magnetization-temperature curves for $Bi_2Sr_{2-x}Na_xCo_2O_y$ samples. The insert in panel show inverse DC-magnetic susceptibility curves for the x=0.075 sample

Figure 9. Hysteresis curves for all $Bi_2Sr_{2-x}Na_xCo_2O_y$ samples, at measured 10 K

Figure 1

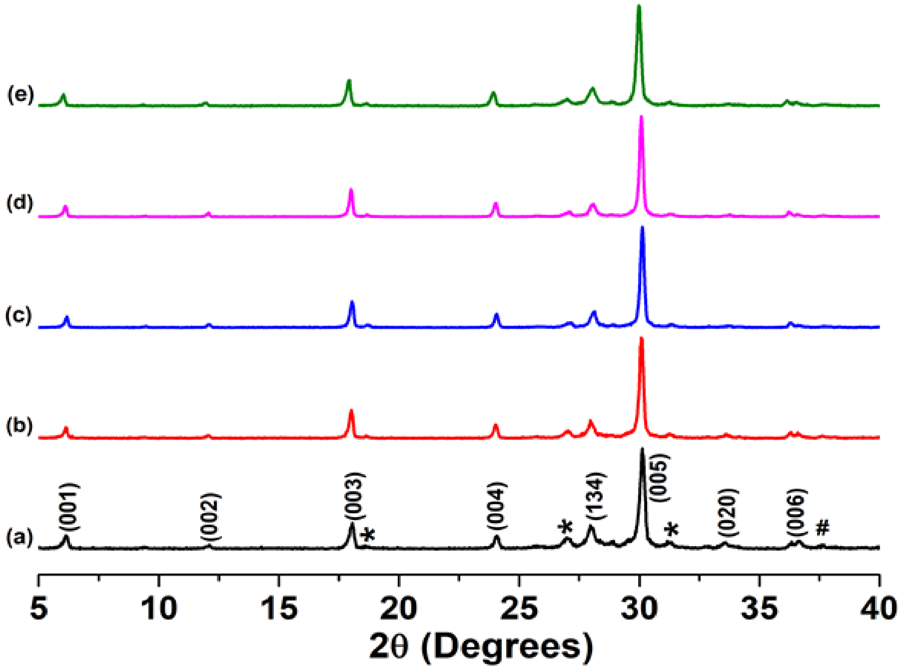
(e)
(d)
(c)
(b)
(a)
(001)
(002)
(003)
*
(004)
*
(134)
(005)
*
(020)
(006)
#
5
10
15
20
25
30
35
40
2θ (Degrees)

Figure 2

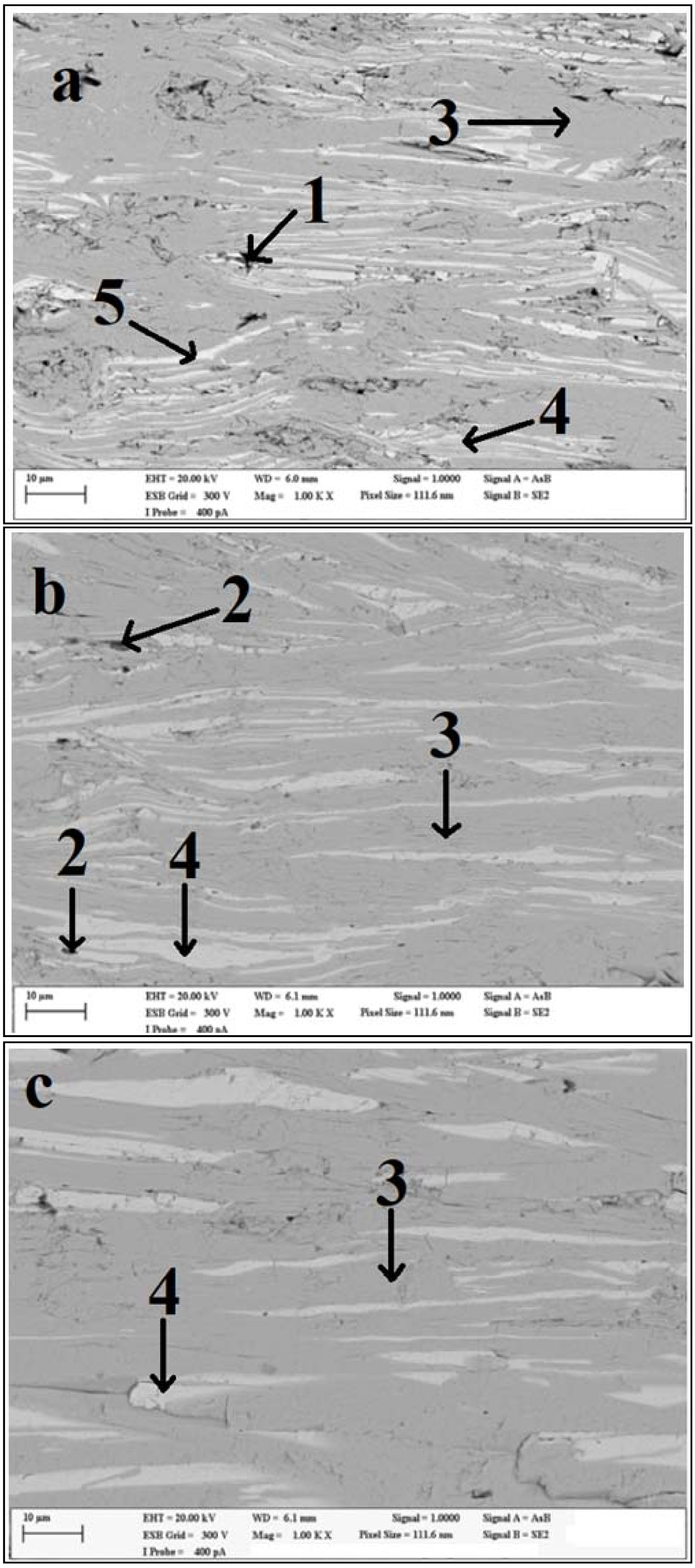
a
3
1
5
4
10 µm
EHT = 20.00 kV
ESB Grid = 300 V
I Probe = 400 pA
WD = 6.0 mm
Mag = 1.00 K X
Signal = 1.0000
Pixel Size = 111.6 nm
Signal A = AsB
Signal B = SE2
b
2
3
2
4
10 µm
EHT = 20.00 kV
ESB Grid = 300 V
I Probe = 400 pA
WD = 6.1 mm
Mag = 1.00 K X
Signal = 1.0000
Pixel Size = 111.6 nm
Signal A = AsB
Signal B = SE2
c
3
4
10 µm
EHT = 20.00 kV
ESB Grid = 300 V
I Probe = 400 pA
WD = 6.1 mm
Mag = 1.00 K X
Signal = 1.0000
Pixel Size = 111.6 nm
Signal A = AsB
Signal B = SE2

Figure 3

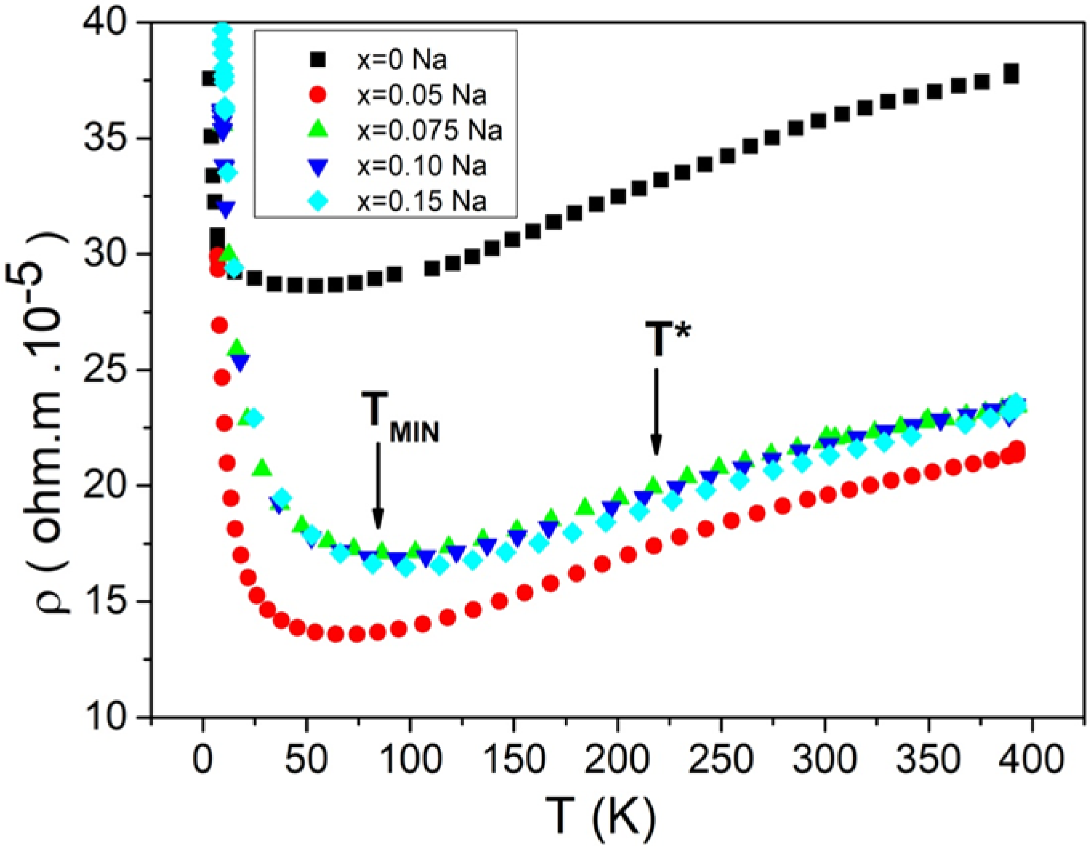
40
35
30
25
20
15
10
ρ (ohm.m .10^{-5})
0
50
100
150
200
250
300
350
400
T (K)
x=0 Na
x=0.05 Na
x=0.075 Na
x=0.10 Na
x=0.15 Na
T$_{MIN}$
T*

Figure 4

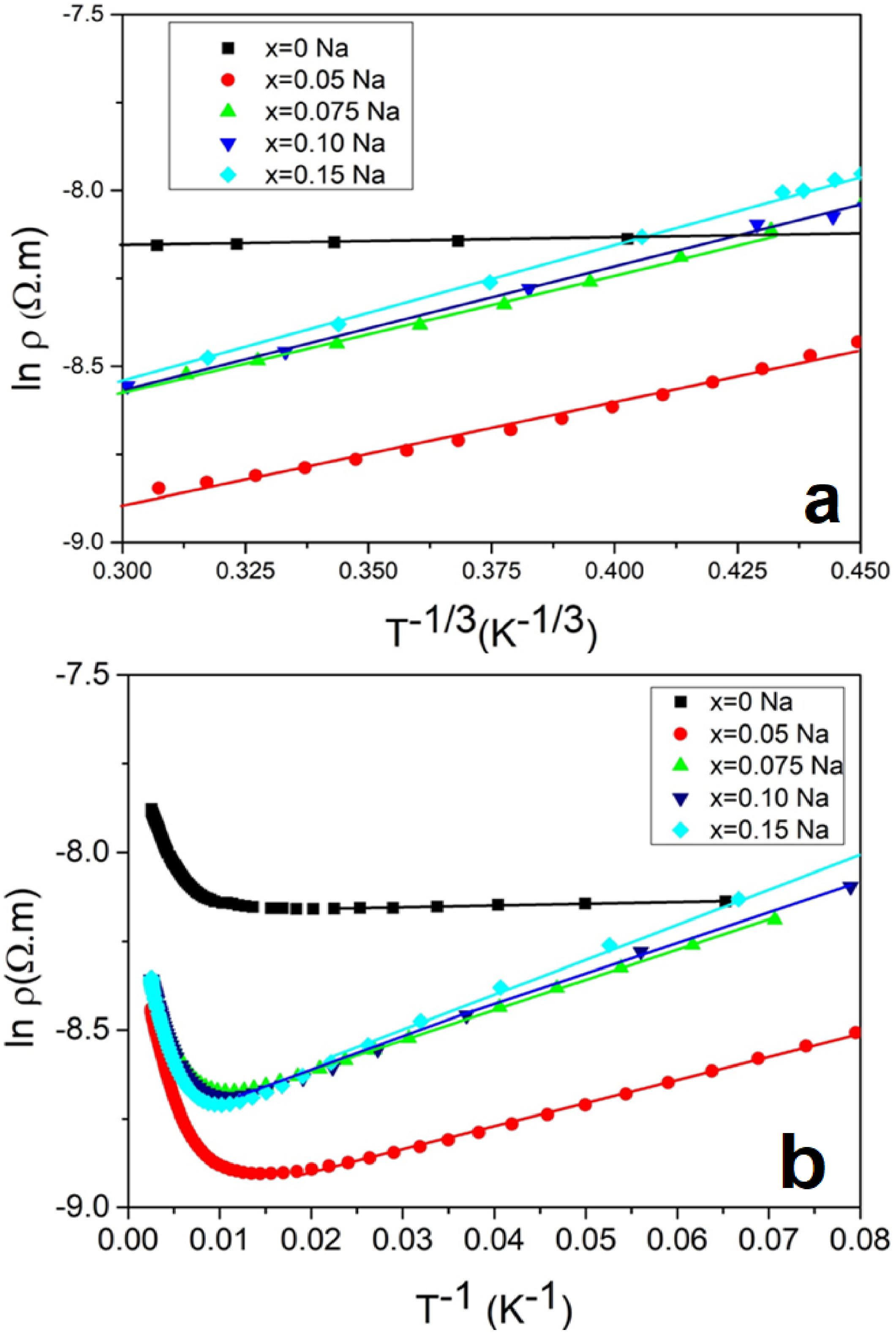
x=0 Na
x=0.05 Na
x=0.075 Na
x=0.10 Na
x=0.15 Na
-7.5
-8.0
-8.5
-9.0
ln ρ (Ω.m)
0.300
0.325
0.350
0.375
0.400
0.425
0.450
$T^{-1/3}(K^{-1/3})$
a
x=0 Na
x=0.05 Na
x=0.075 Na
x=0.10 Na
x=0.15 Na
-7.5
-8.0
-8.5
-9.0
ln ρ(Ω.m)
0.00
0.01
0.02
0.03
0.04
0.05
0.06
0.07
0.08
T^{-1} (K^{-1})
b

Figure 5

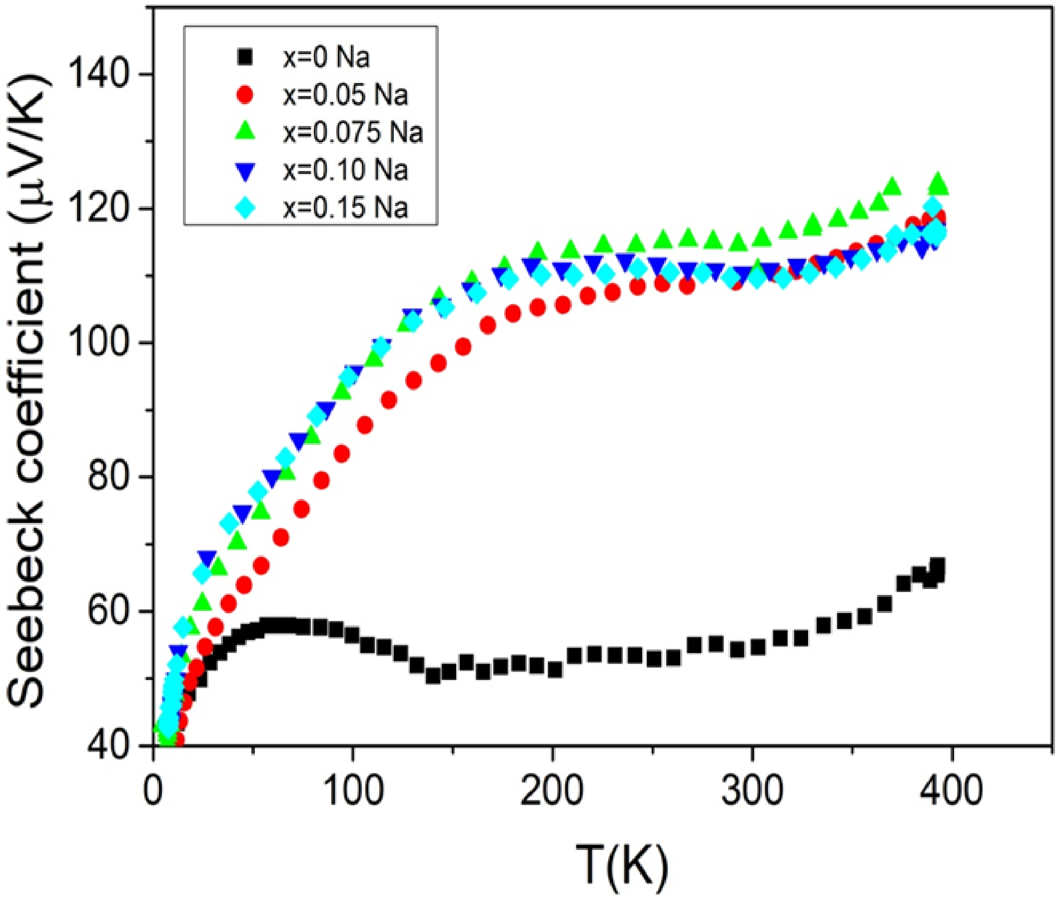
x=0 Na
x=0.05 Na
x=0.075 Na
x=0.10 Na
x=0.15 Na
Seebeck coefficient (μV/K)
140
120
100
80
60
40
0
100
200
300
400
T(K)

Figure 6

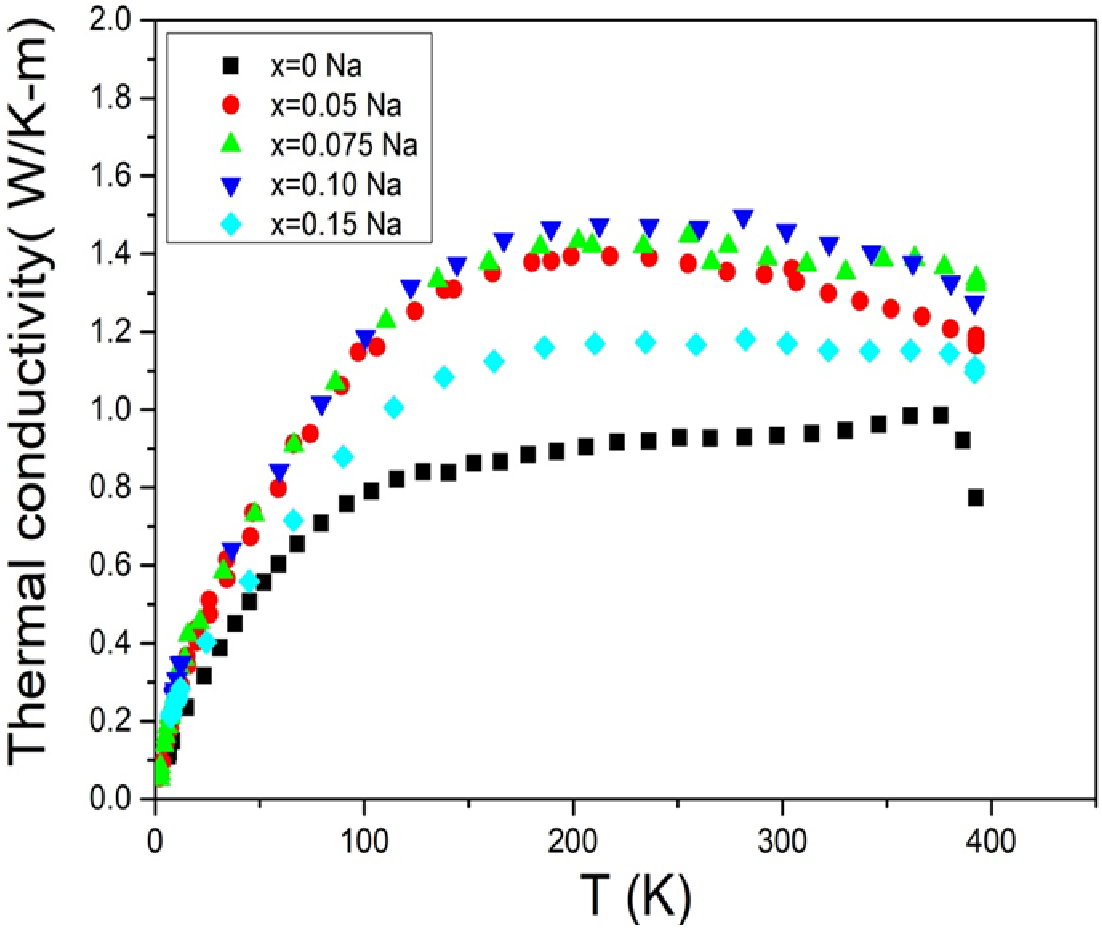
Thermal conductivity(W/K-m)
2.0
1.8
1.6
1.4
1.2
1.0
0.8
0.6
0.4
0.2
0.0
0
100
200
300
400
T (K)
■ x=0 Na
● x=0.05 Na
▲ x=0.075 Na
▼ x=0.10 Na
◆ x=0.15 Na

Figure 7

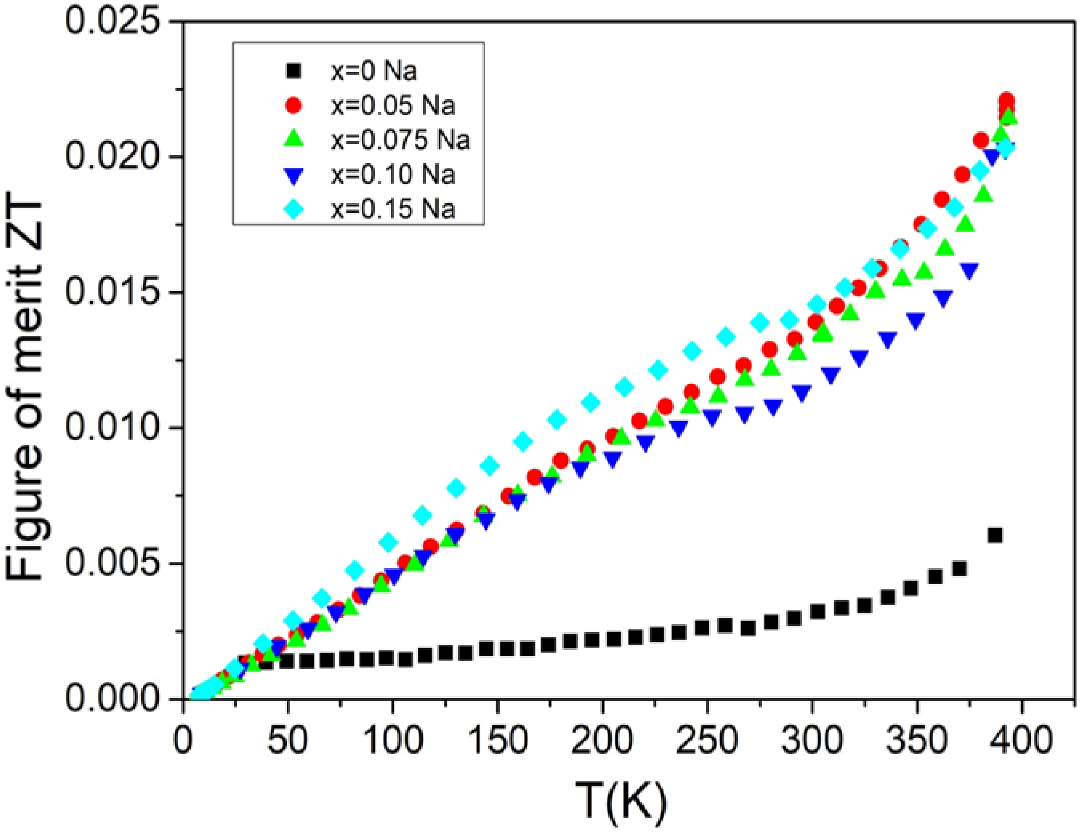
Figure of merit ZT
0.025
0.020
0.015
0.010
0.005
0.000
0
50
100
150
200
250
300
350
400
T(K)
x=0 Na
x=0.05 Na
x=0.075 Na
x=0.10 Na
x=0.15 Na

Figure 8

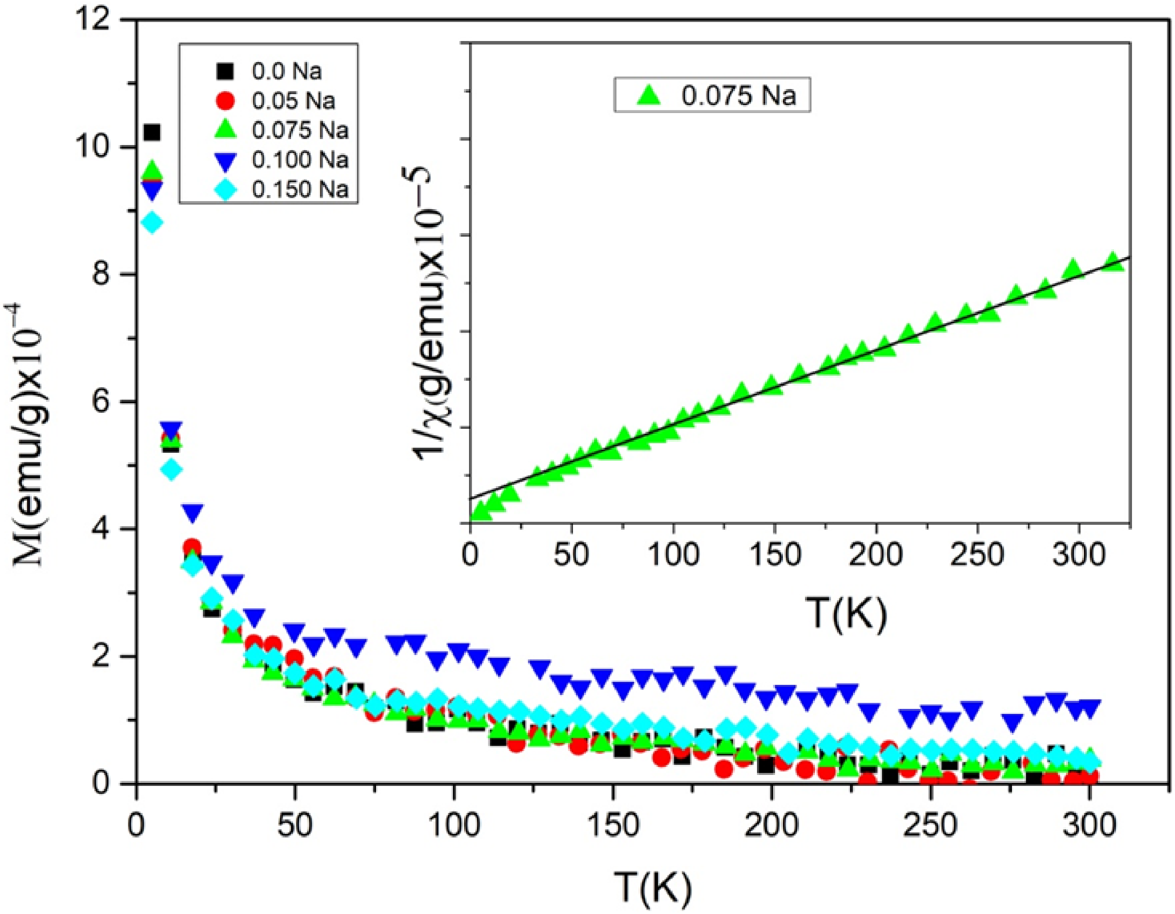

M(emu/g)x10^{-4}
0
2
4
6
8
10
12
0
50
100
150
200
250
300
T(K)
0.0 Na
0.05 Na
0.075 Na
0.100 Na
0.150 Na
1/χ(g/emu)x10^{-5}
0.075 Na
0
50
100
150
200
250
300
T(K)

Figure 9

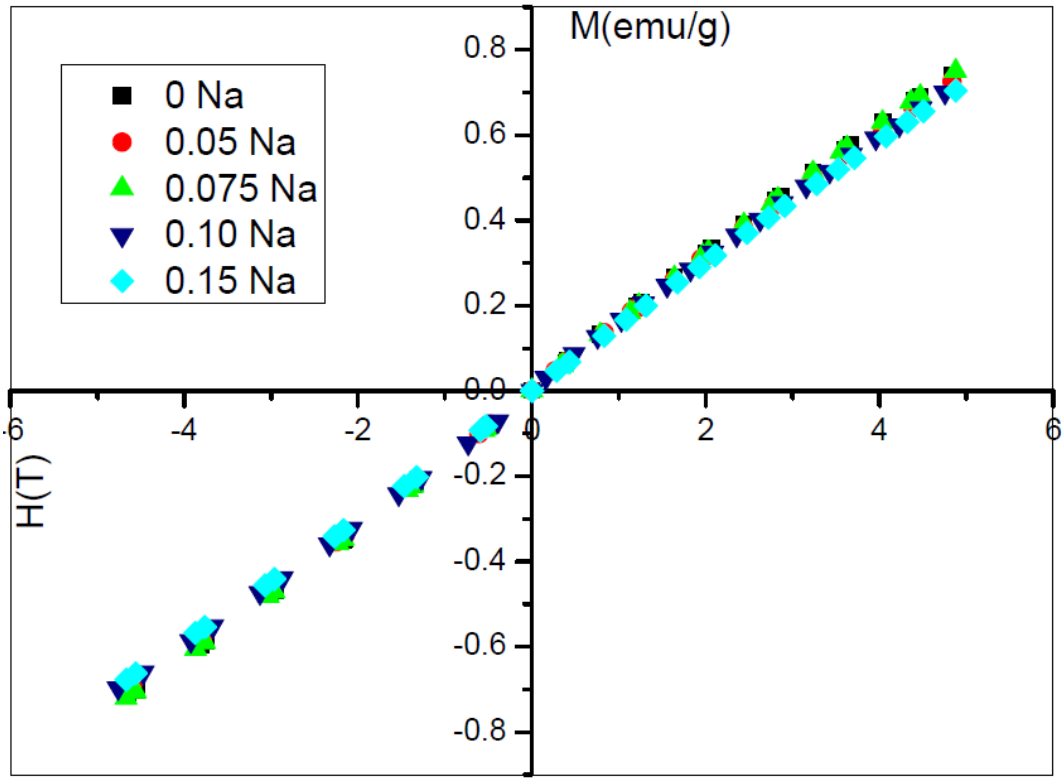
M(emu/g)
H(T)
0 Na
0.05 Na
0.075 Na
0.10 Na
0.15 Na
0.8
0.6
0.4
0.2
0.0
-0.2
-0.4
-0.6
-0.8
-6
-4
-2
0
2
4
6